# Ion and electron spectroscopy of strontium in the vicinity of the two-photon-excited $5p^2\,{}^1S_0$ state

A. Dimitriou* and S. Cohen†

*Atomic and Molecular Physics Laboratory, Physics Department, University of Ioannina, 45110 Ioannina, Greece*

(Received 5 May 2014; published 14 July 2014)

Two-photon ionization of ground-state strontium is investigated experimentally in the 360–370-nm spectral range with dye laser pulses of long (∼ns) duration and low ($\sim 10^{10}$ W cm$^{-2}$) intensity. The $Sr^+$ spectra recorded with linear laser polarization are dominated by the presence of the highly correlated $5p^2\,{}^1S_0$ state and by the even parity $[4d6d]_{J=0,2}$ autoionizing states. The partial $J = 0$ and $J = 2$ two-photon ionization cross sections are recovered from these data along with the spectra obtained with circular polarization. For linear polarization, the observed wavelength dependence of $Sr^+$ production is compared with earlier theoretical work based on the $R$-matrix–multichannel-quantum-defect-theory approach and the agreement is generally found to be quite satisfactory. There are, however, a few, albeit noticeable, discrepancies. The latter motivated us to proceed to a more comprehensive experimental characterization of the examined energy range, by also measuring the kinetic energy and angular distribution of the ejected photoelectrons under linear laser polarization. The shapes of the angular distributions vary rapidly in the neighborhood of each resonance, while these distributions are found to be almost spherically symmetric on the maxima of the sharp $[4d6d]_{J=0}$ lines. On these, and only these, maxima, electron energy spectra reveal the absorption of a third photon, resulting in production of $Sr^+$ into its excited $4d_j$ and $5p_j$ states. The non-negligible $5p_j$ branching ratio reflects the mixing between the $[4d6d]_{J=0}$ states and the $5p^2\,{}^1S_0$ perturber, found to be rather underestimated by the aforementioned theoretical work. Thus, the presently acquired ion and electron spectra as well as the asymmetry parameters obtained by fitting the photoelectron angular distributions provide a stringent test of future theoretical efforts, addressing structure as well as excitation and ionization issues in an improved manner.

DOI: 10.1103/PhysRevA.90.012513 PACS number(s): 33.60.+q, 32.80.Rm, 32.80.Zb, 31.15.vj

## I. INTRODUCTION

Multiphoton-excitation and -ionization processes in multielectron atoms are well suited not only for spectroscopic applications but also for investigations of the response and dynamics of target atoms during their interaction with sufficiently strong laser fields. A great number of such studies were devoted to alkaline-earth-metal atoms, having two valence electrons outside a closed-subshell ionic core. These atoms are characterized by dense manifolds of doubly excited autoionizing states immediately above their first ionization thresholds; that is, their continua are structured and dominated by electron-correlation effects. The employment of multistep and/or nonresonant multiphoton ionization schemes allows excitation of doubly excited states with symmetries which are inaccessible from the $ms^2\,{}^1S_0$ ground states of alkaline-earth-metal atoms via traditional single-photon ionization techniques ($m = 2$, 3, 4, 5, and 6 for Be, Mg, Ca, Sr, and Ba, respectively). Multistep schemes may be considered as one-photon ionization processes out of the last intermediate state involved. The experiments based on these schemes as well as their theoretical analyses focused on the atomic structure in the final doubly excited states, rather than the excitation process itself (see, for example, [1] and references therein).

Single-color multiphoton excitation and ionization of doubly excited states from the ground state of alkaline-earth-metal atoms and without resonant bound intermediate states is experimentally more convenient and was employed recently for efficient ion production and trap loading for quantum optics and metrology applications [2]. Furthermore, single-color experiments frequently offer a much wealthier variety of phenomena, as, for example, the absorption of photons above the first $ms_{1/2}$ ionization thresholds leading to the production of ions into excited states [3]. Moreover, when moderately intense laser fields of long (∼ns) pulse duration are involved, above-threshold photon absorption heavily relies on electron-correlation effects and the presence of autoionizing states, the latter playing the role of resonant or near-resonant intermediate levels. On the contrary, when short (∼ps or ∼fs) and intense pulses are employed, level structure issues are of much less importance and a single-active-electron picture prevails [4]. Consequently, the theoretical interpretation of long-pulse experiments necessitates additional efforts; that is, the electron-correlation-dominated atomic structure and the laser-atom interaction processes need to be adequately considered on a, more or less, equal footing.

The above reasoning explains the continuous interest for detailed studies on nonresonant multiphoton ionization in the vicinity of the low-lying and highly correlated $mp^2\,{}^1S_0$ states, located just above the first $ms_{1/2}$ thresholds. Most attention has been paid to the lighter alkaline-earth-metal atoms Be, Mg, and Ca, and few-photon excitation. Perturbative two-photon-excitation calculations for Be [5] satisfactorily reproduced the experimental results [6]. For the Mg atom good general agreement was found between experimentally acquired and theoretically computed ion spectra for either perturbative two-photon [7–13] or nonperturbative four-photon [14] excitation of the $3p^2\,{}^1S_0$ state. Equally good agreement was obtained for two-photon ionization in the vicinity of the $4p^2\,{}^1S_0$ and neighboring $[3d5d]_{J=0,2}$ and $[3d7s]_{J=2}$ levels of Ca [15,16]. However, for the heavier and much more complex

*Present address: Department of Physics, University of Crete, P.O. Box 2208, 71003 Heraklion, Crete, Greece.

†scohen@uoi.gr

 

Sr atom the comparison between the nonresonant two-photon-excited $5p^2\,{}^1S_0$+$[4d6d]_{J=0,2}$ autoionizing structure [17] (also studied via stepwise excitation [17,18]) and subsequent $R$-matrix–multichannel-quantum-defect-theory (MQDT) calculations [19] was not conclusive. More recent work based on $R$-matrix–Floquet theory employed $LS$-coupled final states [20] and neglected spin-orbit mixing effects. Consequently, a number of resonances which are present in the experimental data did not show up in the computed spectrum.

The above inconclusive results motivated us to examine this energy range of Sr in more detail, using an array of experimental techniques. Thus, apart from recording two-photon $Sr^+$ ion spectra we also measure the photoelectron angular distributions (PADs). Moreover, photoelectron energy analysis shows that, even under our low-laser-intensity conditions ($\sim 10^{10}$ W cm$^{-2}$), above-threshold absorption (ATA) of a third photon occurs on the maxima of specific autoionizing resonances. The presently acquired data, therefore, imply a more complicated situation than that originally anticipated and they are adequate for a comprehensive comparison with subsequent perturbative multiphoton ionization calculations.

The rest of the paper is divided into three sections: In the following section we introduce the excitation scheme and describe the experimental setup and procedure. Next, the $Sr^+$ and electron spectra as well as the photoelectron angular distributions from two- and three-photon ionization of ground-state Sr are presented and discussed. Finally, in the last section a synthesis of all our partial observations as well as our general conclusions and suggestions for further work are given.

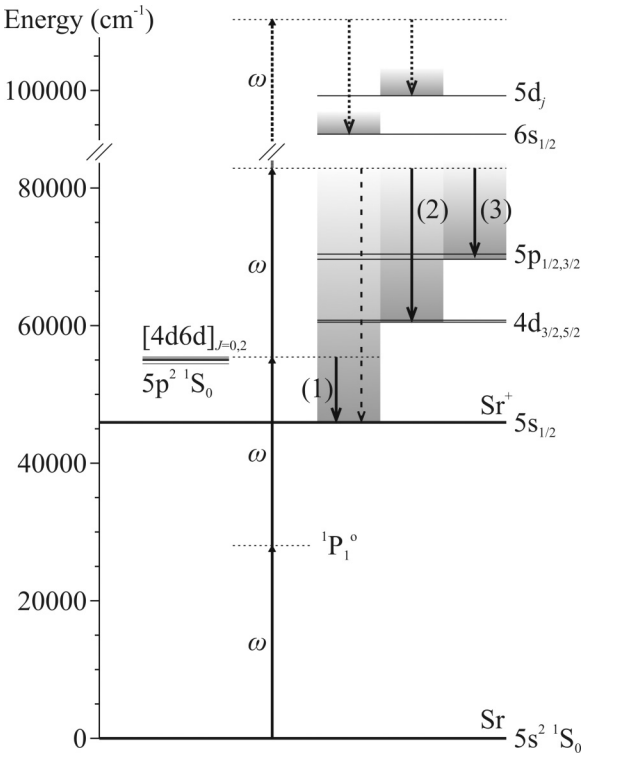


FIG. 1. Partial energy level diagram of Sr along with the multiphoton-excitation scheme. The two-photon-excited autoionizing states and the decay pathways are discussed in the text.

## II. EXPERIMENT

### A. Excitation scheme and ionization pathways

The presently employed multiphoton-excitation and -ionization scheme is shown in Fig. 1. The energy range in the vicinity of the first absorbed photon is characterized by the absence of any resonant state within at least $\pm 5000$ cm$^{-1}$. Nevertheless, the two-photon absorption cross section is dominated by the $5s6p$ state [20]. Furthermore, the $LS$-coupling scheme is valid in this range and virtual intermediate states are of almost pure $^1P_1^o$ character [19]. The absorption of two photons leads to excitation of the $5s\varepsilon s$ and $5s\varepsilon d$ continua and the $5p^2\,{}^1S_0$ and $[4d6d]_{J=0,2}$ autoionizing states. These levels, along with the whole $[4dnd]_{J=0-2}$ Rydberg series and their interactions with the $5pnp$ channels, were experimentally studied via a stepwise, two-color excitation scheme and theoretically analyzed though the $R$-matrix–MQDT approach [17,18]. In fact, an experimental two-photon-excitation $Sr^+$ spectrum of the range studied here was also given in [17]. Nonetheless, a detailed comparison with two-photon $R$-matrix–MQDT computations [19] was not possible because the zero of the experimental ionization signal was arbitrary and the data were too noisy for the line asymmetries to be compared (see [19], Fig. 1, and its caption therein).

The above-threshold absorption of a third photon excites the atom above the $4d_j$ and $5p_j$ thresholds ($V_{i,4d}$ and $V_{i,5p}$, respectively), the immediately higher threshold being the $6s_{1/2}$ one ($V_{i,6s}$). The energy $E$ reached by three photons corresponds to an effective quantum number $\upsilon = [(V_{i,6s}-E)/R_{\rm Sr}]^{1/2} \approx 3$, with respect to this latter threshold (with "$R_{\rm Sr}$" denoting the mass-corrected Rydberg constant). Therefore, the presence of $6sn\ell$ resonances with $n \sim \upsilon$ is quite improbable, while, even if present, they are expected to exhibit very large autoionization widths. Single-photon ionization experiments extending up to $6s_{1/2}$ threshold [21] are in support of the above arguments. We may conclude that this energy range is dominated by continua. Finally, the absorption of a fourth photon would excite the atom above the $5d_j$ and $6s_{1/2}$ thresholds.

The above-described ionization processes may produce several electron groups of different energy. The groups observed in the present work are denoted as (1)–(3) in Fig. 1 and they correspond to the following ionization processes:

$$\mathrm{Sr} + 2\omega \rightarrow \mathrm{Sr}^+(5s_{1/2}) + e^-(\approx 1.1\ \mathrm{eV}), \quad (1)$$

$$\mathrm{Sr} + 3\omega \rightarrow \mathrm{Sr}^+(4d_j) + e^-(\approx 2.8\ \mathrm{eV}), \quad (2)$$

$$\mathrm{Sr} + 3\omega \rightarrow \mathrm{Sr}^+(5p_j) + e^-(\approx 1.6\ \mathrm{eV}), \quad (3)$$

i.e., group (1) is related to atomic ionization at the second-photon level, leaving the ion to the $5s_{1/2}$ $Sr^+$ ground state. Groups (2) and (3) stem from three-photon ionization leaving the ion to its excited $4d_j$ and $5p_j$ ionic states, respectively. Three-photon ionization may also produce ground-state $Sr^+$ (dashed vertical line in Fig. 1) but this process was not observed in the present work. Finally, our data show weak and difficult-to-quantify evidence of four-photon ionization leaving the ion to the $6s_{1/2}$ state (one of the two dotted vertical lines in Fig. 1).

### B. Experimental setup and procedure

The atomic beam apparatus, capable of electron and ion detection, is schematically shown in Fig. 2; it was described recently in some detail [8,22]. Therefore, our presentation here will be brief and we shall emphasize mostly those elements which are relevant to the present study. Strontium vapor is produced in an electrically heated stainless steel oven mounted at the top of a laser-atom interaction chamber that is connected to it through a water-cooled baffle. The vapor passes through a ≈0.5-mm-diameter hole where it is collimated via a ≈15-cm-long stainless steel tube of ≈5 mm inner diameter. The atoms interact with the laser beam at about 3 cm downstream of the tube exit. The chamber is evacuated by a rotary pump and a turbomolecular pump system and is equipped with two liquid nitrogen traps. The achieved background pressure is $\approx 5 \times 10^{-8}$ mbar. The employed oven temperature (640°C–700°C) results in an estimated vapor density of $\sim 10^7$–$10^8$ atoms/cm$^3$ at the laser-atom interaction point. The temperature is continuously monitored by a thermocouple and is kept constant to within 1°C.

The atomic beam interacts at right angles with the laser beam. The latter is provided by a Nd:YAG pumped dye laser (Lamda Physik Scanmate 2EC-400 pumped by Brilliant BW) whose fundamental wavelength lies in the 720–740-nm range. The system operates at a repetition rate of 10 Hz and delivers linearly polarized pulses of ≈0.1 cm$^{-1}$ linewidth and ≈5 ns duration. The radiation wavelength is fairly accurately calibrated by the laser system itself. Nevertheless, a small part of the fundamental dye laser beam is directed to a commercial, Ar-filled, hollow cathode lamp and the resulting optogalvanic signal is used as a secondary absolute wavelength calibration standard. For the two-photon ionization of Sr the fundamental frequency is doubled by a BBO type-III crystal. The second-harmonic radiation pulse energy is controlled by a variable attenuator and it is measured in front of the chamber's entrance fused silica window by a digital joule meter. Its maximum value amounts to ≈1 mJ. The UV laser beam is guided to the chamber by a pair of right-angle prisms. Subsequently, the beam passes through an alpha-BBO Rochon prism polarizer, a double Fresnel rhomb, and a single Fresnel rhomb. The Rochon polarizer purifies the beam's linear polarization from small imperfections caused by the prisms. By rotating the double Fresnel rhomb the polarization may be varied from linear to circular without any lateral displacement or pulse energy variation. PAD recordings (accomplished by rotating the double Fresnel rhomb) are recorded with the single Fresnel rhomb removed. Finally, the beam is focused into the interaction chamber by an $f \approx 10$ cm focal length lens.

The ions and electrons created by the laser-atom interaction are detected perpendicularly to both the atomic and laser beams. The photoelectrons are energy analyzed by an electrostatic 166° spherical sector electron energy analyzer (Comstock AC-902B), operated in the constant transmission energy mode [23] and equipped with an electrostatic lens (Comstock EL-321) for the purpose of maximizing the collected electron signal. The latter is detected by a pair of microchannel plates (MCPs) mounted at the exit of the analyzer. The whole system is placed within a $\mu$-metal box for protection against parasitic magnetic fields. The achieved energy resolution $\Delta E_{\mathrm{FWHM}}/E_{\mathrm{o}}$ is ∼0.8% for transmission energies, $E_{\mathrm{o}}$, in the range 10–30 eV. The angular resolution is found to be ≈3° with the electrostatic lens turned off and ≈4° when the lens is turned on. Apart from this small angular resolution degradation, the lens does not influence the recorded PADs in any other way (as was already pointed out in earlier studies [24]). The $Sr^+$ ions are discriminated against parasitic ionic signals by means of a pulsed time-of-flight (TOF) mass spectrometer placed in tandem with the analyzer. A positive ≈1-kV pulse is applied on a hollow repeller electrode ≈500 ns after the laser pulse. This delay is long enough so that the electron signal has completely decayed. The electric pulse pushes the ions towards a grounded plate with a ≈3 mm diameter hole in its center which is followed by a ≈18-cm-long grounded tube. At the end of the tube ions are detected by another pair of MCPs.

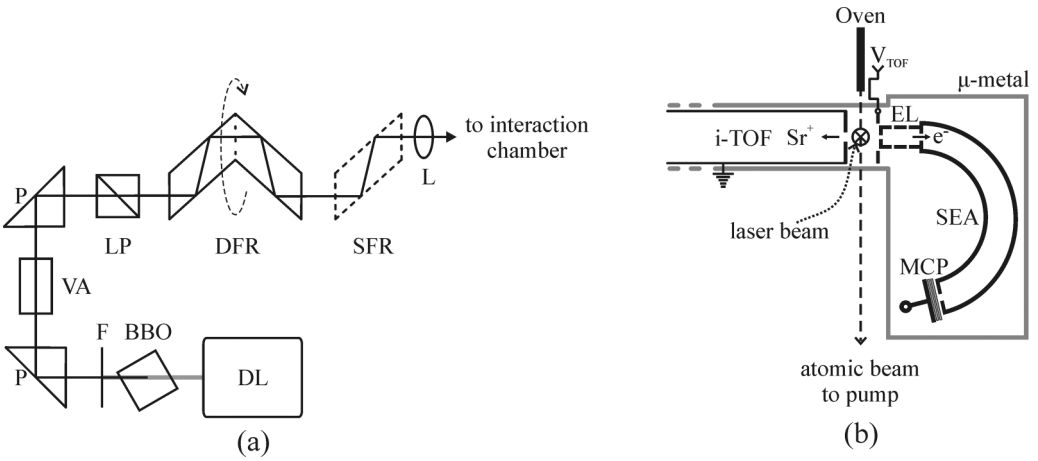


FIG. 2. Schematic drawing of the experimental setup. (a) Optical arrangement. DL: dye laser system; BBO: BBO type-III frequency doubling crystal; F: filter for the suppression of the fundamental wavelength laser beam; P: right-angle prism; VA: variable attenuator; LP: linear polarizer; DFR: double Fresnel rhomb; SFR: single Fresnel rhomb (removed for PAD measurements); L: fused silica lens. (b) Interaction chamber and ion and electron detection. i-TOF: positive ion time-of-flight mass spectrometer; $V_{TOF}$: positive HV pulse. EL: Electrostatic lens; SEA: spherical sector electron energy analyzer; MCP: microchannel plates.

All the voltages required for the operation of the analyzer are provided by a dedicated power supply (Comstock Model ES-101). The latter is driven by a 0–10-V voltage ramp provided by a programmable module (Stanford Research Systems SR245). The module itself is driven by a personal computer through homemade LABVIEW software. The electron and ion signals (either themselves or after they are processed by boxcar integrators) are monitored by a digital oscilloscope and transferred and stored to the personal computer which is connected to the oscilloscope via a GPIB port.

## III. RESULTS AND DISCUSSION

### A. Wavelength dependence of the $Sr^+$ yield

Let us begin our presentation from the two-photon ionization spectra. The latter are shown in Fig. 3(a) for linearly polarized light and in Fig. 3(b) for circularly polarized light. Great care was taken in order to avoid saturation of the $Sr^+$ signal, even on the strongest resonance at ≈360.7 nm. To this purpose, both measurements were acquired with a low-UV-laser power density, $I \approx 2 \times 10^{10}$ W cm$^{-2}$.

We discuss first the data shown in Fig. 3(a). According to the dipole selection rules, two-photon excitation or ionization

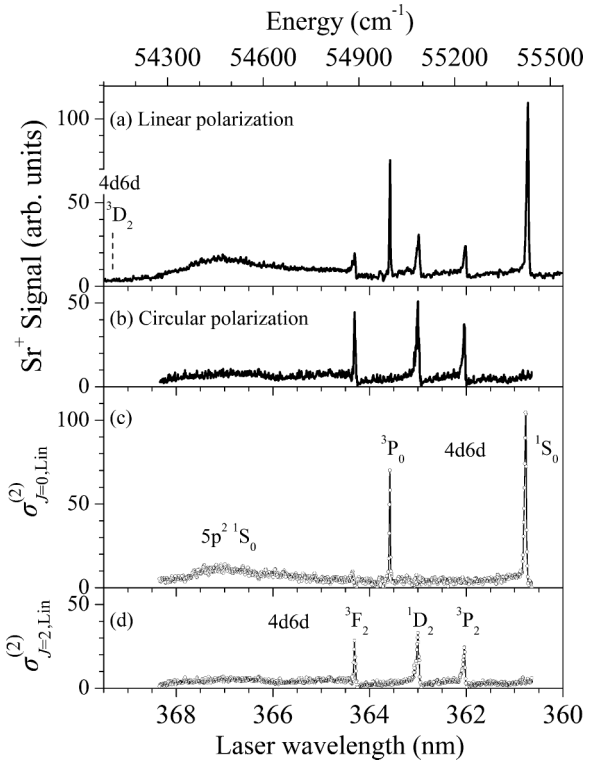


FIG. 3. Experimental $Sr^+$ spectra recorded as a function of UV laser wavelength with (a) linear laser polarization ($J = 0$ and 2 final states) and (b) circular polarization ($J = 2$ final states only). Apart from the different polarizations the two spectra were recorded under identical conditions and laser power density $I \approx 2 \times 10^{10}$ W cm$^{-2}$. (c) $\sigma^{(2)}_{J=0,\mathrm{Lin}}$ and (d) $\sigma^{(2)}_{J=2,\mathrm{Lin}}$ partial two-photon cross sections for linear polarization (both in arbitrary units), estimated as explained in the text and using spectra (a) and (b). The $y$ scales of all plots (a)–(d) can be compared to each other. Details on level assignments are given in the text.

out of the $5s^2\ ^1S_0$ ground state and with linearly polarized light leads to final states of even parity and total angular momentum $J = 0$ and $J = 2$ ($M_J = 0$). Indeed, apart from the weak background $Sr^+$ signal (originating from nonresonant two-photon ionization to the available $5s\varepsilon s$ and $5s\varepsilon d$ continua), the spectrum consists of a broad resonance at ≈367 nm attributed to the $5p^2\ ^1S_0$ doubly excited state [17], and a number of fairly sharp lines stemming from the $[4d6d]_{J=0,2}$ autoionizing levels [17,18]. Our wavelength calibration procedure provides energy level positions and autoionization widths of the observed resonances which agree with earlier experimental values to within ≈1.5 cm$^{-1}$. The only exception concerns the maximum of the $5p^2\ ^1S_0$ line, which is found to be blueshifted by about 25 cm$^{-1}$ with respect to the level position given in [17]. This is not an alerting discrepancy, however, if one considers the ≈230 cm$^{-1}$ width of this resonance. Such a large width is a consequence of the strong coupling between the $5p^2\ ^1S_0$ state and the $5s\varepsilon s$ continuum into which it autoionizes. In turn, the strength of the coupling is explained by the fact that it is induced by the strong dipole term in the multipole expansion of the dielectronic interaction between the two valence electrons. On the contrary, all $[4d6d]_{J=0,2}$ states exhibit comparable and small (2–6 cm$^{-1}$) autoionization widths, because of the weak quadrupolar $[4dnd]_{J=0} \rightarrow 5s\varepsilon s$ and $[4dnd]_{J=2} \rightarrow 5s\varepsilon d$ autoionization processes [19].

All the resonances are $LS$ labeled in Fig. 3. The $LS$-coupling scheme, however, is appropriate solely for the $5p^2\ ^1S_0$ state, while approximately suitable for the $[4d6d]_{J=0}$ states [19]. The appearance in Fig. 3(a) of the $4d6d\ ^3P_0$ resonance is to be attributed to its mixing with the $4d6d\ ^1S_0$ state and the $5p^2\ ^1S_0$ perturber. As for the $[4d6d]_{J=2}$ resonances, the $LS$-coupling scheme is completely inappropriate and this is manifested by the excitation of both singlet ($^1D_2$) and triplet ($^3P_2$, $^3F_2$) states. It is interesting to note that the remaining $4d6d\ ^3D_2$ member appears to be weakly excited in the theoretically calculated two-photon spectrum [19] (Fig. 1, therein), while it is unobservable in either our experimental data or the earlier ones [17]. Its expected location (known from the relevant stepwise, two-color excitation experiment [18]) is noted in Fig. 3(a) with a dashed vertical line. Its disappearance is reminiscent of a quite similar situation encountered in Ca [16] and attributed to the mixing among the $[3dnd]_{J=2}$ states. For Sr these levels were labeled in [18] using $jj$ coupling, and the available $4d_{3/2}nd_{3/2}$, $4d_{5/2}nd_{3/2}$, $4d_{3/2}nd_{5/2}$, and $4d_{5/2}nd_{5/2}$ series were denoted as $|nd_{--}\rangle$, $|nd_{+-}\rangle$, $|nd_{-+}\rangle$ and $|nd_{++}\rangle$, respectively. Furthermore, the analysis showed that one $[4d6d]_{J=2}$ member has 100% $|6d_{--}\rangle$ character, while another member has 97% $|6d_{++}\rangle$ character. On the contrary, the $|6d_{+-}\rangle$ and $|6d_{-+}\rangle$ members are found to be strongly coupled, their mutual mixing amounting to about 60%–40%. Let us denote as $|6l\rangle$ and $|6h\rangle$ the low- and high-energy member of mixed character, respectively, and assume, for the sake of a qualitative discussion, equal (50%–50%) mixing. Then we have

$$|6l\rangle \approx 2^{-1/2}[|6d_{+-}\rangle \pm |6d_{-+}\rangle], \tag{4}$$

$$|6h\rangle \approx 2^{-1/2}[|6d_{+-}\rangle \mp |6d_{-+}\rangle], \tag{5}$$

with a remaining sign ambiguity for each one of them. Considering the $\Delta S = 0$ excitation selection rule applying to $LS$

coupling and the fact that the geometric $LS$–$jj$ transformation yields equal percentages of $^1D$ character for the $|6d_{+-}\rangle$ and $|6d_{-+}\rangle$ components [25], the second-photon transition matrix elements from a pure $^1P_1^o$ intermediate state are written as

$$\langle ^1P|\hat{D}|6h(\text{or } l)\rangle \propto f_{\pm}\langle ^1P|\hat{D}|6^1D\rangle, \tag{6}$$

where $\hat{D}$ stands for the dipole transition operator. In Eq. (6) the factors $f_{\pm}$ are $f_+ = 2$ and $f_- = 0$. Consequently, one member exhibits a pure triplet character and should not be two-photon excited. Indeed, this is the $|6l\rangle$ one (that is, the $^3D_2$ $LS$-labeled state) for which the negative sign applies. In fact, a 60%–40% mutual mixing could lead to its weak two-photon excitation. Nevertheless, this line did not appear in our spectra even for higher-laser-power densities leading to saturated $Sr^+$ signals.

Further comparison between theory [19] and the present experiment reveals good agreement. Specifically, the relative resonant and nonresonant contributions, the relative strength among spectral lines, and the observed stronger excitation of $[4d6d]_{J=0}$ resonances as compared to the $[4d6d]_{J=2}$ ones are all well reproduced by theory. Equally good agreement is found for all the mildly asymmetric Fano profiles, except for the profile of the $4d6d\ ^1S_0$ resonance. For the latter, the experimentally observed profile asymmetry (characterized by its two-photon Fano parameter [26] $q^{(2)}$) is found to be reversed with respect to that predicted by either $R$-matrix–MQDT [19] or $R$-matrix–Floquet theory [20] calculations. The parameter $q^{(2)}$ is proportional to the transition matrix element connecting the initial state to the bound part of the autoionizing state and inversely proportional to the corresponding matrix element for the continuum part. Furthermore, $q^{(2)}$ is inversely proportional to the matrix element expressing the mutual coupling between bound and continuum parts [26]. Consequently, a reversed sign of $q^{(2)}$ implies that the sign (phase) of at least one of these matrix elements is different from that computed in [19]. While $Sr^+$ spectra may bring the problem to our attention, they cannot provide further information about its origin. To that purpose, a comparison between theoretical and experimental PADs might be more useful.

The dipole selection rules for excitation with circularly polarized light predict that only $J = 2$ ($|M_J| = 2$) even parity final states should be observed and this is confirmed by the data of Fig. 3(b). We note in this figure that at the minima of the asymmetric Fano profiles of all $J = 2$ resonances the $Sr^+$ signal is quasizero. Apart from the locations of these minima the nonresonant ionization to $5s\varepsilon d$ continua is weak but nonzero over the whole recorded spectral range, including the locations of the unexcited $J = 0$ resonances. Taking advantage of the identical recording conditions, the unsaturated data of Figs. 3(a) and 3(b) can be used for a decomposition of the spectrum recorded with linear polarization to partial $J = 0$ and $J = 2$ ionization cross sections. The total two-photon cross sections for linearly ($\sigma^{(2)}_{\text{tot,Lin}}$) and circularly ($\sigma^{(2)}_{\text{tot,Circ}}$) polarized light are given by [27]

$$\sigma^{(2)}_{\text{tot,Lin}} = \tfrac{1}{3}\sigma^{(2)}_{J=0,\text{unp}} + \tfrac{2}{15}\sigma^{(2)}_{J=2,\text{unp}}, \tag{7a}$$

$$\sigma^{(2)}_{\text{tot,Circ}} = \tfrac{1}{5}\sigma^{(2)}_{J=2,\text{unp}}, \tag{7b}$$

where $\sigma^{(2)}_{J=0,\text{unp}}$ and $\sigma^{(2)}_{J=2,\text{unp}}$ denote the corresponding partial cross sections for unpolarized light. The system of Eqs. (7a) and (7b) leads to an estimate of $\sigma^{(2)}_{J=0,\text{unp}}$ and $\sigma^{(2)}_{J=2,\text{unp}}$, and subsequently to an estimate of the partial cross sections for linearly polarized light, $\sigma^{(2)}_{J=0,\text{Lin}} = \sigma^{(2)}_{J=0,\text{unp}}/3$ and $\sigma^{(2)}_{J=2,\text{Lin}} = 2\sigma^{(2)}_{J=2,\text{unp}}/15$. These two last quantities are shown in Figs. 3(c) and 3(d), respectively. The latter is simply a rescaled version of the spectrum of Fig. 3(b), in order to account for the different angular factors applying to each polarization. Of higher interest is the fairly successful decomposition of $\sigma^{(2)}_{J=0,\text{Lin}}$ [Fig. 2(c)], which shows small distortions only on the maxima of a couple of $J = 2$ levels. The decomposition to partial cross section amounts to the maximum information that can be extracted from the ion spectra. Under certain assumptions, PADs can also provide information on this decomposition. This will be discussed in more detail in the relevant subsection.

### B. Electron energy analysis

The electron energy spectrum recorded at ≈365.3 nm (on the blue side of the $5p^2\ ^1S_0$ resonance maximum) is given in Fig. 4(a). The spectrum was acquired at an angle $\theta = 0°$ between the linear laser polarization vector and the direction of detection. It consists of a single line at ≈1.1 eV, attributed to the two-photon ionization process of Eq. (1) where the $Sr^+$ ion is left to its $5s_{1/2}$ ground state. This single-line picture is typical over the whole wavelength range studied here, but with two important exceptions: Additional lines appear in the electron spectrum when the laser wavelength is tuned on the maxima of the $4d6d\ ^3P_0$ [Fig. 4(b)] and $^1S_0$ [Fig. 4(c)] resonances (and only on them). The highest-energy peak at ≈2.8 eV is attributed to process (2) of Fig. 1, i.e., three-photon ionization leaving $Sr^+$ to its excited $4d_j$ levels. The second peak at ≈1.6 eV also stems from three-photon ionization where $Sr^+$ is left in this case to its excited $5p_j$ levels [Eq. (3)]. For the two three-photon peaks to be comfortably recorded, the spectra of Figs. 4(b) and 4(c) were acquired by employing the maximum available laser intensity, $\approx 4 \times 10^{10}$ W cm$^{-2}$. Otherwise, these two lines were observable but rather faint. Finally, on the maximum of the $4d6d\ ^1S_0$ resonance, there may be another quite weak electron peak at ≈2.1 eV, corresponding to four-photon absorption leaving $Sr^+$ in its $6s_{1/2}$ excited state. Nevertheless, the amplitude of this peak is comparable to our signal's noise. Therefore, we cannot be conclusive about its presence and it will not be discussed any further.

From the spectra of Figs. 4(b) and 4(c) as well as the PADs recorded on each electron peak we may estimate the relevant angle-integrated branching ratios. It turns out that on the maximum of the $4d6d\ ^1S_0$ resonance the relative populations left to the $5s_{1/2}$ ground state, the $4d_j$, and the $5p_j$ excited states of $Sr^+$ are ≈91%, ≈4%, and ≈5%, respectively. The corresponding relative populations when the laser is tuned to the maximum of the $^3P_0$ resonance are ≈84%, ≈10%, and ≈6%. Hence, the amount of ionic population found in excited states after absorption of a third photon is substantial. Moreover, the $4d_j$ and $5p_j$ branching ratios are comparable. Obviously, the above findings are not to be attributed to a high-laser-intensity effect. Instead, taking into account the absence of three-photon-excited autoionizing states mentioned earlier, it is evident that they are a consequence of sizable

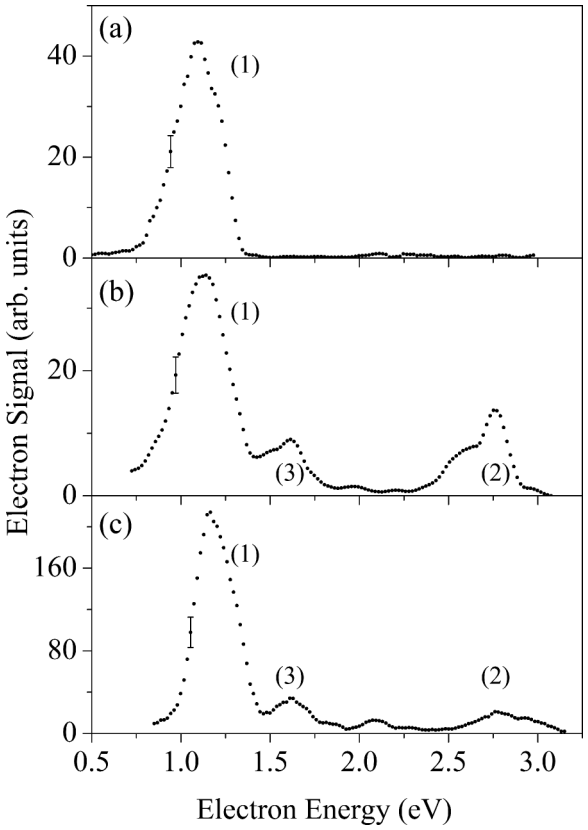


FIG. 4. Electron energy spectra acquired at different wavelengths and with linear laser polarization pointing towards the direction of detection ($\theta = 0°$). The pass energy of the electrostatic analyzer was set at $E_o = 30$ eV. (a) Spectrum recorded at $\lambda \approx 365.3$ nm (on the blue side of $5p^2\,{}^1S_0$ resonance) for laser power density $I \approx 2 \times 10^{10}$ W cm$^{-2}$. Only the process described by Eq. (1) is observed. (b), (c) Spectra on the maxima of the $4d6d\,{}^3P_0$ ($\lambda \approx 363.5$ nm) and $4d6d\,{}^1S_0$ ($\lambda \approx 360.7$ nm) lines, respectively, for $I \approx 4 \times 10^{10}$ W cm$^{-2}$. The processes described by Eqs. (2) and (3) are also observed. In plot (c) an additional electron peak is visible, whose energy ($\sim$2.1 eV) corresponds to four-photon ionization and the ion left to its $6s_{1/2}$ state (see Fig. 1). This peak, however, is quite weak and not fully reproducible. The curves drawn in (a)–(c) were obtained after smoothing the recorded data. The signal error bars, given for a single point of each plot, correspond to the maximum (and typical) amplitude of the residual (nonsmoothed minus smoothed) curve. The electron energy scales were calibrated using known two-photon resonant, three-photon ionization processes of Xe atom [24], recorded under unsaturated and space-charge-free conditions.

correlation effects among the two excited valence electrons at the two-photon level. A pure $4d6d$ configuration would be efficiently one-photon coupled solely to the $4d\varepsilon\ell$ continua with $\ell = p$, $f$, and $h$, while a pure $5pnp$ configuration would be coupled solely to the $5p\varepsilon\ell'$ continua with $\ell' = s$, $d$, and $g$. Therefore, the decay to the $5p_j$ thresholds is by itself a clear manifestation of configuration mixing caused by electron-correlation effects. Thus, both the $^1S_0$ and the $^3P_0$ $4d6d$ states should present important admixtures of $[5pnp]_{J=0}$ character. The energetically nearest $5pnp$ member is, of course, the $5p^2\,{}^1S_0$ state, for which theory predicts a rather small admixture, of the order of 10% [19]. The next $5pnp$ member ($5p6p\,{}^3P_0$) is located more than 3500 cm$^{-1}$ above the energy range studied here. While this resonance was not observed experimentally in [17], it was theoretically predicted that its character is diluted into a large number of $[4dnd]_{J=0}$ series members. Therefore, at present its influence on the observed branching ratios cannot be excluded.

### C. Photoelectron angular distributions

#### 1. Two-photon ionization

Angular distributions of photoelectrons from two-photon ionization are recorded over the whole wavelength range of Fig. 3(a). At each wavelength the transmission energy of the electron analyzer is set at the maximum of the peak of process (1) and the electron signal is recorded as a function of the angle $\theta$ between the linear laser polarization and the direction of electron detection. The wavelength steps are unequal, being smaller close to sharp $J = 0$ and $J = 2$ resonances. The oven temperature (and, hence, the atomic density at the interaction point) is chosen so as to avoid any apparent space-charge effects. To that purpose, for each wavelength it is reduced to a value resulting in quasisymmetric electron line profiles, exhibiting the instrumental linewidths. The data are fitted to the form [28]

$$\frac{d\sigma_{\rm Lin}^{(N)}}{d\Omega} \propto 1 + \sum_{k=1}^{N} \frac{\beta_{2k}^{(N)}}{\beta_0^{(N)}} P_{2k}(\cos\theta), \tag{8a}$$

where $P_{2k}$ are Legendre polynomials and $N$ is the number of absorbed photons (here $N = 2$). For unsaturated electron

TABLE I. Parameters $\beta_{2k}^{(2)}/\beta_0^{(2)}$, $k$ = 1–2 [Eq. (8a) with $N$ = 2], determined from the fits of PADs from two-photon ionization of ground-state Sr and for laser intensity $I \approx 2 \times 10^{10}$ W cm$^{-2}$. The estimated uncertainty of absolute wavelength values and wavelength differences is $\approx$0.05 nm and $\approx$0.01 nm, respectively.

| λ (nm) | $\beta_2^{(2)}/\beta_0^{(2)}$ | $\beta_4^{(2)}/\beta_0^{(2)}$ | λ (nm) | $\beta_2^{(2)}/\beta_0^{(2)}$ | $\beta_4^{(2)}/\beta_0^{(2)}$ |
|---|---|---|---|---|---|
| 359.52 | 1.8 ± 0.1 | 0.8 ± 0.1 | 363.50 | 1.6 ± 0.1 | 1.2 ± 0.1 |
| 360.02 | 2.3 ± 0.2 | 1.1 ± 0.1 | 363.51 | 1.7 ± 0.1 | 0.5 ± 0.1 |
| 360.52 | 2.1 ± 0.1 | 1.5 ± 0.1 | 363.53 | 0.28 ± 0.05 | 0.02 ± 0.06 |
| 360.62 | 1.1 ± 0.1 | 1.3 ± 0.1 | 363.56 | 1.0 ± 0.1 | 0.3 ± 0.1 |
| 360.72 | 0.20 ± 0.05 | 0.04 ± 0.06 | 363.58 | 1.58 ± 0.1 | 0.9 ± 0.1 |
| 360.82 | 1.6 ± 0.1 | 0.8 ± 0.1 | 363.63 | 1.9 ± 0.2 | 1.0 ± 0.2 |
| 361.02 | 2.5 ± 0.2 | 1.2 ± 0.1 | 363.69 | 1.99 ± 0.09 | 1.09 ± 0.08 |
| 361.27 | 2.2 ± 0.2 | 1.5 ± 0.2 | 363.91 | 1.9 ± 0.1 | 1.1 ± 0.1 |
| 361.44 | 2.2 ± 0.1 | 1.0 ± 0.1 | 364.21 | 2.3 ± 0.2 | 1.2 ± 0.1 |
| 361.59 | 2.3 ± 0.1 | 1.31 ± 0.09 | 364.41 | 2.5 ± 0.1 | 1.3 ± 0.1 |
| 361.69 | 1.7 ± 0.1 | 1.0 ± 0.1 | 364.87 | 2.3 ± 0.1 | 1.2 ± 0.1 |
| 361.95 | 2.4 ± 0.1 | 1.8 ± 0.1 | 365.12 | 2.4 ± 0.1 | 1.1 ± 0.1 |
| 362.19 | 2.3 ± 0.2 | 1.5 ± 0.1 | 365.23 | 2.4 ± 0.1 | 0.84 ± 0.08 |
| 362.44 | 2.1 ± 0.1 | 1.2 ± 0.1 | 365.40 | 2.3 ± 0.1 | 0.73 ± 0.09 |
| 362.67 | 1.8 ± 0.1 | 0.67 ± 0.09 | 365.90 | 2.1 ± 0.1 | 0.59 ± 0.08 |
| 362.90 | 2.3 ± 0.2 | 1.7 ± 0.1 | 366.40 | 2.0 ± 0.1 | 0.52 ± 0.08 |
| 363.02 | 2.5 ± 0.1 | 1.5 ± 0.1 | 366.91 | 1.32 ± 0.07 | 0.26 ± 0.06 |
| 363.17 | 2.5 ± 0.1 | 1.2 ± 0.1 | 367.40 | 0.84 ± 0.04 | 0.35 ± 0.04 |
| 363.34 | 2.4 ± 0.2 | 1.4 ± 0.1 | 367.90 | 0.45 ± 0.05 | 0.66 ± 0.06 |
| 363.43 | 2.1 ± 0.2 | 1.2 ± 0.1 | 368.90 | 0.32 ± 0.05 | 1.32 ± 0.07 |
| 363.48 | 2.3 ± 0.2 | 1.3 ± 0.2 | | | |

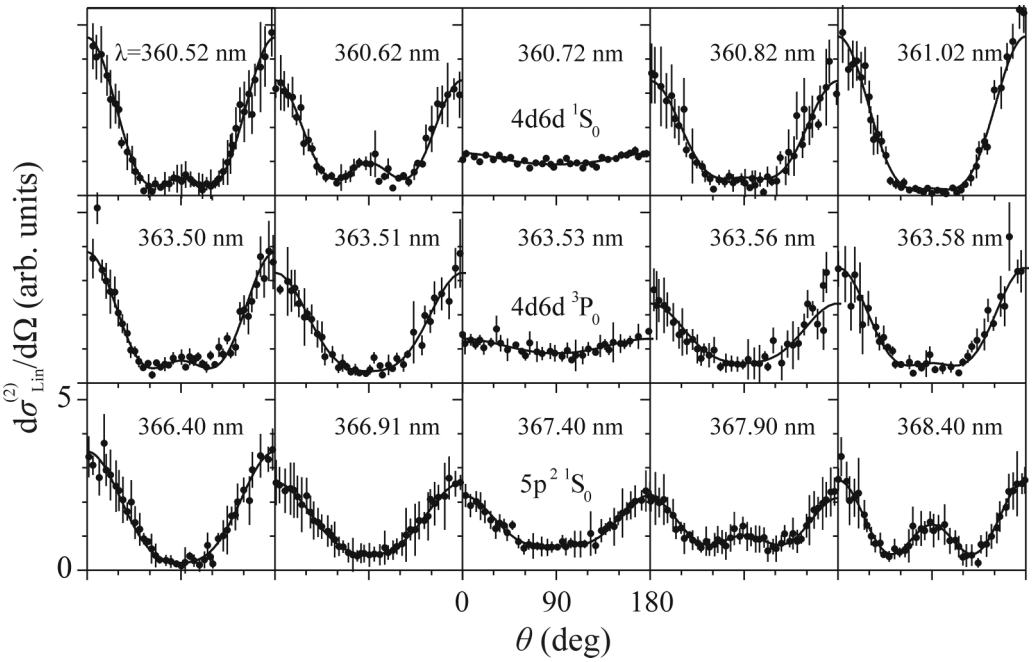


FIG. 5. Selected experimental and fitted PADs from two-photon ionization of ground-state Sr [process of Eq. (1)], for $I \approx 2 \times 10^{10}$ W cm$^{-2}$. The quoted error bars are the standard deviation of the experimental data accumulated over a few thousand laser shots. Vertical as well as horizontal scales are the same for all graphs. Each row shows the PADs in the vicinity of a given $J = 0$ final doubly excited state, i.e., the $4d6d\ ^1S_0$ (upper row), the $4d6d\ ^3P_0$ (middle row), and the $5p^2\ ^1S_0$ one (bottom row). The maximum of the latter broad resonance occurs at ≈367 nm. On the maxima of the two $[4d6d]_{J=0}$ resonances the PADs are almost spherically symmetric.

signals the parameter $\beta_0^{(N)}$ of Eq. (8a) is given by

$$\beta_0^{(N)} = \frac{\sigma^{(N)}_{\text{tot,Lin}}}{4\pi}; \tag{8b}$$

i.e., it is proportional to the total ionization cross section.

The fitted ratios $\beta_{2k}^{(2)}/\beta_0^{(2)}$ $(k = 1,2)$ for all PAD measurements are assembled in Table I. Figure 5 shows selected experimental and fitted PADs in the vicinity of each one of the three $J = 0$ resonances. The wavelength dependence of the PAD shapes is remarkable. A number of PADs exhibit a local maximum at $\theta = 90°$ which is a manifestation of considerable contribution from the $5s\varepsilon d$ continua [8,22]. On the contrary, the absence of the $\theta = 90°$ lobe signals the relative dominance of the $5s\varepsilon s$ continuum. More striking, however, is the difference between the on-resonance PADs corresponding to $[4d6d]_{J=0}$ and $5p^2\ ^1S_0$ states, respectively. The former are quasi–spherically symmetric, as expected for a final $J = 0$ level [29], while the latter is asymmetric (with no $\theta = 90°$ lobe). In fact, the behavior of the PADs within the broad wavelength range covered by the $5p^2\ ^1S_0$ resonance is quite reminiscent of experimental observations [8] and theoretical predictions [11,13] for the two-photon-excited $3p^2\ ^1S_0$ state of Mg. This behavior can be more clearly visualized in Fig. 6, where the spectrum recorded with linear polarization [Fig. 6(a)] is plotted along with the ratios $\beta_2^{(2)}/\beta_0^{(2)}$ [Fig. 6(b)] and $\beta_4^{(2)}/\beta_0^{(2)}$ [Fig. 6(c)]. Indeed, the significant variation of $\beta_2^{(2)}/\beta_0^{(2)}$ within the range 366 nm≤λ≤369 nm and the minimum of $\beta_4^{(2)}/\beta_0^{(2)}$ on the maximum of the broad $5p^2\ ^1S_0$ line (≈367 nm) follows closely the variation of the corresponding ratios for the Mg case ([13], Fig. 1 therein), albeit with somewhat different magnitudes. Finally, for the remaining part of the spectrum, the ratios $\beta_{2k}^{(2)}/\beta_0^{(2)}$ vary quite rapidly in the neighborhood of every autoionizing resonance, the dominant features being, of course, their sharp dips reflecting the quasi–spherically symmetric PADs on the maxima of $[4d6d]_{J=0}$ lines.

Evidently, a thorough analysis of such complicated wavelength dependence of the $\beta_{2k}^{(2)}/\beta_0^{(2)}$ ratios requires a theoretical calculation that would be even more advanced than the existing earlier one [19] which, as already mentioned above, is found to be in slight disagreement with our $Sr^+$ spectra. In the absence of such a theory, at present we may either fit the data using a sufficiently detailed MQDT model or analyze them after making some simplifying assumptions. Much of the complication stems from final-state singlet-triplet mixing and configuration interaction effects. Moreover, there are three available continua, namely, $5s\varepsilon s\ ^1S_0$ (or $5s_{1/2}\varepsilon s_{1/2}$) and $5s\varepsilon d\ ^1D_2$ and $^3D_2$ (or $5s_{1/2}\varepsilon d_{3/2}$ and $5s_{1/2}\varepsilon d_{5/2}$). Using $jj$-coupled final states, both $J = 2$ continua need to be considered and this leads to fairly complicated expressions for the asymmetry parameters $\beta_{2k}^{(2)}$ [11]. Then, an MQDT model including all available continua and the minimum required number of bound channels would involve ~40 MQDT parameters. Their number being so high, it is quite improbable that their values would be reliably and uniquely determined by a fitting procedure. Consequently, a global fit to all our data would produce results of questionable significance. On the other hand, the analysis can be considerably simplified by recalling that (i) $J = 2$ resonances exhibit asymmetric Fano profiles on the minima of which the $Sr^+$ signal is quasizero [see Fig. 3(b)]. This fact implies that these states are coupled to a single $J = 2$ continuum [26], while the other available continuum is

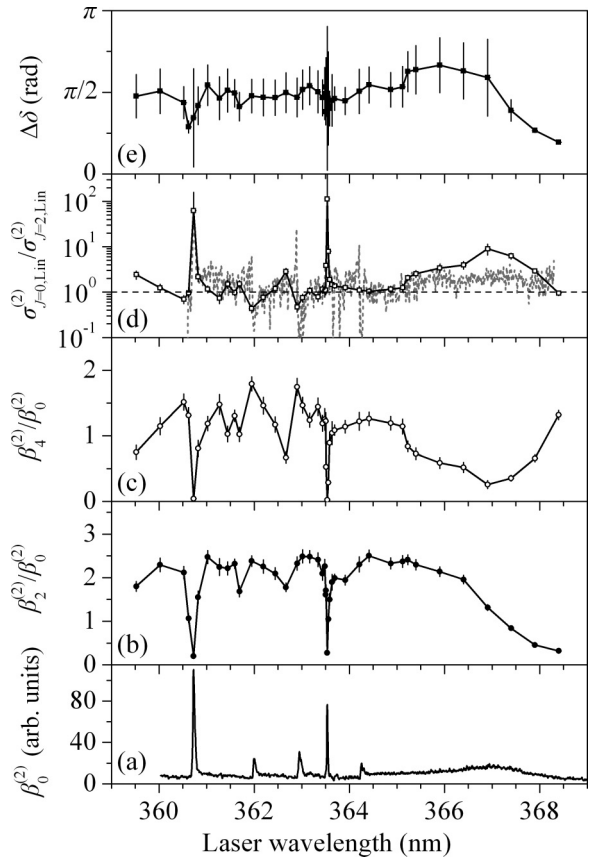


FIG. 6. (a) Reproduction of the $Sr^+$ spectrum given in Fig. 3(a) and recorded with linear laser polarization. It represents $\sigma^{(2)}_{\mathrm{tot,Lin}}$ [Eq. (7a)], which, in turn, is proportional to $\beta^{(2)}_0$ [Eq. (8b)]. (b) UV laser wavelength dependence of the asymmetry parameter ratio $\beta^{(2)}_2/\beta^{(2)}_0$, determined by fitting the PADs from two-photon ionization of ground-state Sr to Eq. (8a). (c) The same as in (b) for the ratio $\beta^{(2)}_4/\beta^{(2)}_0$. In (b) and (c) the symbols are connected by straight lines. (d) Partial cross-section ratio $\sigma^{(2)}_{J=0,\mathrm{Lin}}/\sigma^{(2)}_{J=2,\mathrm{Lin}}$, as estimated via the ratios $\beta^{(2)}_{2k}/\beta^{(2)}_0$ and Eqs. (9a)–(9c) (white squares) and by the ratio of the $Sr^+$ spectra of Figs. 3(c) and 3(d) (gray dashed line). The latter exhibit "spikes" on the locations of $J = 2$ resonances due to the quasizero signal minima of their Fano profiles. (e) Phase difference $\Delta\delta = \delta_2 - \delta_0$ between $5s\varepsilon s\,{}^1S_0$ and $5s\varepsilon d\,{}^1D_2$ continua. $\Delta\delta$ (assumed to be positive) is estimated through the ratios $\beta^{(2)}_{2k}/\beta^{(2)}_0$ and Eqs. (9a)–(9c).

not excited. (ii) Virtual intermediate states at the one-photon level exhibit an almost pure ${}^1P^o_1$ character [19]. These two pieces of information validate the assumption of *LS*-coupled continua and imply that only the ${}^1D_2$ one is two-photon excited. Hence, as far as $J = 2$ final (autoionizing as well as continuum) states are concerned and irrespective of the most appropriate coupling scheme, two-photon excitation probes solely their ${}^1D_2$ character. Consequently, we may adopt the *LS*-coupling scheme and employ the corresponding expressions for the asymmetry parameters $\beta^{(2)}_{2k}$, which are much simpler. Specifically, we have [13,29]

$$\beta^{(2)}_0 = \left|D^{(2)}_{{}^1S}\right|^2 + \left|D^{(2)}_{{}^1D}\right|^2, \tag{9a}$$

$$\beta^{(2)}_2 = \tfrac{10}{7}\left|D^{(2)}_{{}^1D}\right|^2 - 2\times\sqrt{5}\left|D^{(2)}_{{}^1S}\right|\left|D^{(2)}_{{}^1D}\right|\cos[\Delta\delta + \Delta\eta], \tag{9b}$$

$$\beta^{(2)}_4 = \tfrac{18}{7}\left|D^{(2)}_{{}^1D}\right|^2, \tag{9c}$$

where $D^{(2)}_{{}^1S}$ and $D^{(2)}_{{}^1D}$ denote reduced two-photon dipole matrix elements connecting Sr ground state to $J = 0$ and $J = 2$ continua, respectively. These elements may be put in the form

$$D^{(2)}_{{}^1L} = \left|D^{(2)}_{{}^1L}\right|\exp[i(\delta_\ell + \eta_\ell)] \tag{10}$$

($L = \ell$), where $\eta_\ell$ is the Coulomb phase of the outgoing electron of angular momentum $\ell$ to the ionization channel $5s\varepsilon\ell$ [11], and $\delta_\ell$ denotes the short-range scattering phase shift which includes resonant and nonresonant contributions. By inspection of Eqs. (7a) and (8b) the squared matrix elements are given by $|D^{(2)}_{{}^1S}|^2 = \sigma^{(2)}_{J=0,\mathrm{Lin}}/4\pi$ and $|D^{(2)}_{{}^1D}|^2 = \sigma^{(2)}_{J=2,\mathrm{Lin}}/4\pi$, i.e., in terms of the partial excitation cross sections. Finally, the difference $\Delta\eta$ is given by [30]

$$\Delta\eta = \eta_2 - \eta_0 = \pi + \arg\Gamma(3 + i/k) - \arg\Gamma(1 + i/k), \tag{11}$$

and depends on the wave number $k = [(E - V_{i,5s})/R_{\mathrm{Sr}}]^{1/2}$ associated with the $5s_{1/2}$ ionization threshold. Accordingly, we have $\Delta\delta = \delta_2 - \delta_0$.

By means of expressions (9)–(11) and the above definitions, the measured $\beta^{(2)}_{2k}/\beta^{(2)}_0$ ratios may provide the ratio $\sigma^{(2)}_{J=0,\mathrm{Lin}}/\sigma^{(2)}_{J=2,\mathrm{Lin}}$ and the phase difference $\Delta\delta$. The latter quantity can only be determined via PAD measurements. The cross-section ratio, however, can also be determined from the decomposition to partial ionization cross sections achieved through the $Sr^+$ spectra obtained with linear and circular laser polarization, that is, by dividing the data of Fig. 3(c) by the data of Fig.3(d). These two independently determined $\sigma^{(2)}_{J=0,\mathrm{Lin}}/\sigma^{(2)}_{J=2,\mathrm{Lin}}$ ratios are superimposed in Fig. 6(d). They are found to be in fair agreement with each other, except for the region around the $5p^2\,{}^1S_0$ resonance where the PAD-extracted data are higher by a factor $\sim$3. The origin of this difference is unclear as yet. Nevertheless, the ratio extracted from the PADs appears to be more reliable, because it follows closely the profile of the broad $5p^2\,{}^1S_0$ line. The general characteristic of $\sigma^{(2)}_{J=0,\mathrm{Lin}}/\sigma^{(2)}_{J=2,\mathrm{Lin}}$ is the dominance of each partial cross section on the locations of the respective resonances for each $J$. Otherwise the off-resonance cross sections are of comparable magnitude. Finally, the phase difference $\Delta\delta$ is shown in Fig. 6(e). Its variation is more noticeable near the $J = 0$ resonances than the $J = 2$ ones. The small sensitivity of $\Delta\delta$ in the vicinity of the sharp $J = 2$ lines may reflect either the approximate character of our treatment or/and indicate the need of a higher density of experimental points with respect to the one employed here. However, it can be concluded with enough confidence that, "on the average," the two continua are dephased by $\sim\pi/2$.

### 2. *Three-photon ionization*

As mentioned above, three-photon ionization is observed solely on the maxima of $[4d6d]_{J=0}$ resonances. The corresponding PADs and their fits using Eq. (8a) with $N = 3$ are shown in Fig. 7. The fitted $\beta^{(3)}_{2k}/\beta^{(3)}_0$ ratios ($k = 1 - 3$) are listed in Table II, where it is evident that $\beta^{(3)}_6/\beta^{(3)}_0$ values are quite small (quasizero if the quoted error bars are taken into account). Recalling that $\beta^{(N)}_{2N}$ heavily depends on the magnitude of $J = N$ partial cross section [12,13], we may anticipate that the contributions of the highest $\ell$ continua

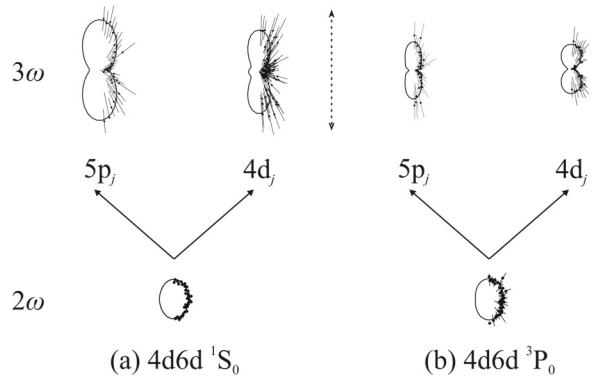


FIG. 7. Experimental (points) and fitted (lines) polar plots of PADs from two-photon ($2\omega$) and three-photon ($3\omega$) ionization at the maxima of (a) $4d6d\ ^1S_0$ and (b) $4d6d\ ^3P_0$ resonances. The vertical dashed double-arrowed line indicates the linear laser polarization direction. The plots do not have the same radial scale. The $2\omega$ case ($I \approx 2 \times 10^{10}$ W cm$^{-2}$) refers to the ionization pathway of Eq. (1), while in the $3\omega$ case ($I \approx 4 \times 10^{10}$ W cm$^{-2}$) there are two pathways leaving the ion either to its $4d_j$ state [Eq. (2)] or its $5p_j$ state [Eq. (3)].

[$4d\varepsilon h$ and $5p\varepsilon g$ for the processes of Eqs. (2) and (3), respectively] are negligible. Furthermore, of all three-photon PADs, only the $4d6d\ ^1S_0 \rightarrow 4d\varepsilon\ell$ one exhibits a local maximum at $\theta = 90°$. The existence of this lobe implies a non-negligible contribution from the $4d\varepsilon f$ partial wave while, in all other cases, the lowest $\ell$ continua ($4d\varepsilon p$ and $5p\varepsilon s$, respectively) appear to be the dominant ones.

## IV. SYNTHESIS AND CONCLUSION

We have studied the ionization processes involved in the vicinity of the two-photon-excited $5p^2\ ^1S_0$ and neighboring $[4d6d]_{J=0,2}$ autoionizing states. The study has been based on ion and electron spectroscopy as well as PAD recordings from two- and three-photon ionization of ground-state Sr. We now combine the above-presented partial observations for drawing our conclusions as well as bringing out a number of open questions.

To begin with, let us comment on the asymmetric profile of the $4d6d\ ^1S_0$ resonance, whose two-photon Fano parameter sign has been experimentally found to be negative, while both earlier theoretical treatments predicted a positive sign [19,20]. Furthermore, a negative sign was predicted in [20] for higher, $n>6$, $4dnd\ ^1S_0$ members, while the $q$ reversal exhibited solely by the $4d6d\ ^1S_0$ resonance was attributed to its strong interaction and subsequent mixing with the $5p^2\ ^1S_0$ state. This strong mixing is also supported by our electron energy spectra on the maximum of the $4d6d\ ^1S_0$ resonance, revealing that three-photon ionization leads to comparable branching ratios for the $4d_j$ and $5p_j$ thresholds. On the one hand, comparable branching ratios imply a mixing higher than that computed in [19] ($\sim$10%), while such a very large mixing is expected to be detrimental as far as ATA is concerned, due to the large autoionization decay of the $5p^2\ ^1S_0$ state. These rather conflicting pieces of information signal the need for new theoretical efforts. The latter should absolutely take into account singlet-triplet mixing and electron-electron–correlation effects, the latter resulting in configuration interaction without any $q$ reversal for the $4d6d\ ^1S_0$ resonance. These efforts should also predict the disappearance of the $4d6d\ ^3D_2$ line. Hence, the presently acquired, higher-quality $Sr^+$ spectra obtained under either linear or circular laser polarization, along with our PAD data, allow for much more stringent tests for any future theoretical treatment.

TABLE II. Parameters $\beta_{2k}^{(3)}/\beta_0^{(3)}$, $k = 1$–3 [Eq. (8a) with $N = 3$], determined from the fits of PADs from three-photon ionization of ground-state Sr on the maxima of $[4d6d]_{J=0}$ resonances and for laser intensity $I \approx 4 \times 10^{10}$ W cm$^{-2}$. The estimated uncertainty of absolute wavelength values is $\approx$0.05 nm.

| Sr level | λ (nm) | $Sr^+$ level | $\beta_2^{(3)}/\beta_0^{(3)}$ | $\beta_4^{(3)}/\beta_0^{(3)}$ | $\beta_6^{(3)}/\beta_0^{(3)}$ |
|---|---|---|---|---|---|
| $4d6d\ ^1S_0$ | 360.72 | $4d_j$ | $1.0 \pm 0.1$ | $0.9 \pm 0.2$ | $0.2 \pm 0.2$ |
| | | $5p_j$ | $1.13 \pm 0.08$ | $0.28 \pm 0.09$ | $0.1 \pm 0.1$ |
| | | $4d_j$ | $1.4 \pm 0.2$ | $0.0 \pm 0.1$ | $0.0 \pm 0.2$ |
| $4d6d\ ^3P_0$ | 363.53 | $5p_j$ | $1.2 \pm 0.1$ | $0.3 \pm 0.1$ | $0.3 \pm 0.2$ |

Another interesting observation is that, under our low laser intensity and long-pulse conditions, ATA is observed solely on the maxima of $[4d6d]_{J=0}$ resonances. This could be simply a consequence of the fact that these resonances are the strongest among the $4d6d$ manifold and they have quite small autoionization widths, i.e., long lifetimes favoring the absorption of the third photon. On the other hand, excitation of the $[4d6d]_{J=2}$ lines is considerably weaker but they exhibit comparably small widths. Therefore, it appears that, although the resonant character of the process is a necessary ingredient for ATA, it is not the dominant factor as far as the observed difference is concerned. Thus, the remaining causes responsible for this difference are the higher excitation efficiency of $[4d6d]_{J=0}$ resonances and their quasi–spherically symmetric angular distributions. Particularly for the latter, it would be quite interesting to theoretically examine whether the high efficiency of ATA out-of-spherically-symmetric states is an observation of more general significance, or is simply specific to the studied atomic system and energy range.

Finally, as mentioned above, ATA with laser pulses of $\sim$ns duration is strongly linked to resonantly excited autoionizing states, i.e., it is dominated by electron-correlation effects. Furthermore, earlier studies with ns pulses [14,31,32] showed that ATA is favored when low-photon-energy radiation (as compared to the single- and double-ionization thresholds) is employed, in order to induce multiply resonant excitations among these autoionizing states. The above arguments prompt for further experimental studies along two directions. First, an electron spectroscopy study using the fundamental laser wavelength is in order. Such radiation of $\sim$ns duration is capable of exciting the $5p^2\ ^1S_0$ state by four photons and of inducing multiple excitation and ATA [32]. Second, the role of pulse duration (and intensity) on the resonant or quasiresonant excitation of autoionizing states needs to be examined. Note that short-pulse ($\sim$ps and $\sim$fs duration) photon absorption above the first ionization threshold (that is, the well-known Above-Threshold-Ionization (ATI) process [33]) occurs even without any resonant structure embedded in the continuum. In other words, it is a single-active-electron effect [4]. Therefore it would be quite interesting to observe the interplay and gradual dominance of the single-active-electron picture over

the electron-correlation-dominated one as the pulse duration is decreased. We are currently conducting electron spectroscopy experiments along these two directions.

## ACKNOWLEDGMENTS

The authors are grateful to F. Robicheaux and A. Lyras for their valuable suggestions and comments. The experiment was performed at the Central Laser Facility of the University of Ioannina. This research has been cofinanced by the European Union [European Social Fund (ESF)] and Greek national funds through the Operational Program "Education and Lifelong Learning" of the National Strategic Reference Framework (NSRF) Research Funding Program: THALES. Investing in knowledge society through the European Social Fund.

[1] M. Aymar, C. H. Greene, and E. Luc-Koening, Rev. Mod. Phys. **68**, 1015 (1996).
[2] E. Kirilov and S. Putterman, Eur. Phys. J. D **54**, 683 (2009); S. Removille, R. Dubessy, B. Dubost, Q. Glorieux, T. Coudreau, S. Guibal, J.-P. Likforman, and L. Guidoni, J. Phys. B: At. Mol. Opt. Phys. **42**, 154014 (2009).
[3] P. Lambropoulos, P. Maragakis, and J. Zhang, Phys. Rep. **305**, 203 (1998).
[4] M. J. Nandor, M. A. Walker, L. D. Van Woerkom, and H. G. Muller, Phys. Rev. A **60**, R1771 (1999); G. D. Gillen, M. A. Walker, and L. D. Van Woerkom, *ibid.* **64**, 043413 (2001).
[5] M. T. Smith, K. T. Taylor, and C. W. Clark, J. Phys. B: At. Mol. Opt. Phys. **25**, 3985 (1992).
[6] C. W. Clark, J. D. Fassett, T. B. Lucatorto, L. J. Moore, and W. W. Smith, J. Opt. Soc. Am. B **2**, 891 (1985).
[7] R. E. Bonanno, C.W. Clark, and T.B. Lucatorto, Phys. Rev. A **34**, 2082 (1986); Y. L. Shao, C. Fotakis, and D. Charalambidis, *ibid.* **48**, 3636 (1993).
[8] A. Dimitriou, S. Cohen, and A. Lyras, J. Phys. B: At. Mol. Opt. Phys. **44**, 135001 (2011).
[9] R. Moccia and P. Spizzo, J. Phys. B: At. Mol. Opt. Phys. **21**, 1145 (1988); Phys. Rev. A **39**, 3855 (1989); S. Mengali and R. Moccia, J. Phys. B: At. Mol. Opt. Phys. **29**, 1597 (1996).
[10] F. Robicheaux and B. Gao, Phys. Rev. A **47**, 2904 (1993).
[11] E. Luc-Koenig, A. Lyras, J.-M. Lecomte, and M. Aymar, J. Phys. B: At. Mol. Opt. Phys. **30**, 5213 (1997).
[12] A. Reber, F. Martín, H. Bachau, and R.S. Berry, Phys. Rev. A **68**, 063401 (2003).
[13] L. A. Nikolopoulos, Phys. Rev. A **71**, 033409 (2005).
[14] I. Liontos, A. Bolovinos, S. Cohen, and A. Lyras, Phys. Rev. A **70**, 033403 (2004).
[15] C. McKenna and H. W. van der Hart, J. Phys. B: At. Mol. Opt. Phys. **36**, 1627 (2003).
[16] S. Cohen, I. Liontos, A. Bolovinos, A. Lyras, S. Benec'h, and H. Bachau, J. Phys. B: At. Mol. Opt. Phys. **39**, 2693 (2006).
[17] M. Kompitsas, S. Goutis, M. Aymar, and P. Camus, J. Phys. B: At. Mol. Opt. Phys. **24**, 1557 (1991).
[18] S. Goutis, M. Aymar, M. Kompitsas, and P. Camus, J. Phys. B: At. Mol. Opt. Phys. **25**, 3433 (1992).
[19] E. Luc-Koenig, M. Aymar, J.-M. Lecomte, and A. Lyras, J. Phys. B: At. Mol. Opt. Phys. **31**, 727 (1998).
[20] M. Madine and H. W. van der Hart, J. Phys. B: At. Mol. Opt. Phys. **38**, 1895 (2005).
[21] M. Aymar, J.-M. Lecomte, C. C. Chu, H. S. Fung, H. H. Wu, and T. S. Yih, J. Phys. B: At. Mol. Opt. Phys. **31**, 5135 (1998).
[22] A. Dimitriou, S. Cohen, A. Lyras, and I. Liontos, J. Phys. B: At. Mol. Opt. Phys. **45**, 205003 (2012).
[23] D. Roy and D. Tremblay, Rep. Prog. Phys. **53**, 1621 (1990).
[24] S. J. Bajic, R. N. Compton, X. Tang, and P. Lambropoulos, Phys. Rev. A **44**, 2102 (1991).
[25] E. U. Condon and G. H. Shortley, *The Theory of Atomic Spectra* (Cambridge University Press, Cambridge, 1970), p. 294.
[26] U. Fano, Phys. Rev. **124**, 1866 (1961).
[27] S. Cohen, M. Aymar, A. Bolovinos, M. Kompitsas, E. Luc-Koenig, H. Mereu, and P. Tsekeris, Eur. Phys. J. D **13**, 165 (2001).
[28] P. Lambropoulos, Adv. At. Mol. Phys. **12**, 87 (1976); S. J. Smith and G. Leuchs, **24**, 157 (1988), and references therein.
[29] F. Robicheaux (private communication).
[30] B. Carre, P. R. Fournier, D. Porterat, H. Lagadec, F. Gounand, and M. Aymar, J. Phys. B: At. Mol. Opt. Phys. **27**, 1027 (1994).
[31] I. Liontos, S. Cohen, and A. Lyras, J. Phys. B: At. Mol. Opt. Phys. **43**, 095602 (2010).
[32] I. Liontos, S. Cohen, and A. Bolovinos, J. Phys. B: At. Mol. Opt. Phys. **41**, 045601 (2008).
[33] P. Agostini, F. Fabre, G. Mainfray, G. Petite, and N. K. Rahman, Phys. Rev. Lett. **42**, 1127 (1979).